In-plane thermal conductivity and the applicability of the Wiedemann-Franz Law in dilute AlCu thin films

Sara Makarem[1], Shivashree Gowda[2], Ramya Mohan[2], Saman Zare[2], Md. Nazmun Sadat Khan[5], Ian A. Brummel[1], Chung T. Ma[5], Md. Shafkat Bin Hoque[2], Daniel Hirt[2], Md. Rafiqul Islam[2], Joseph Poon[1,5], Jon F. Ihlefeld[1,3], Giovanni Esteves[4], Ethan A. Scott[2], Patrick E. Hopkins[1,2,5, a)]

[1.] Department of Materials Science and Engineering, University of Virginia, Charlottesville, VA 22904, USA

[2.] Department of Mechanical and Aerospace Engineering, University of Virginia, Charlottesville, VA 22904, USA

[3.] Charles L. Brown Department of Electrical and Computer Engineering, University of Virginia, Charlottesville, Virginia 22904, USA

[4.] Microsystems Engineering, Science and Applications (MESA), Sandia National Laboratories, Albuquerque, NM 87123

[5.] Department of Physics, University of Virginia, Charlottesville, VA 22904, USA

[a)] **Author to whom correspondence should be addressed:** phopkins@virginia.edu

Table of Contents

Supplementary Note 1. Sample Preparation and Characterization

Four AlCu films (thicknesses ~24, 53, 98, and 174 nm) were deposited on 150 mm silicon wafers coated with a 1.5 µm thick SiO_2 layer via pulsed vapor deposition (PVD). Deposition conditions included an argon (Ar) gas flow rate of 30–50 sccm, 9 kW DC power, and a chamber pressure of 3 mTorr maintained at 20 °C. (ref) Film thicknesses were confirmed using X-ray reflectometry (XRR).

1. Grain Size Distribution

Topographic atomic force microscopy (AFM) was performed using an Asylum Cypher S AFM in AC mode. The resulting AFM micrographs were post-processed using Gwyddion software to level the background and apply false coloring. Figure S1 (a)–(d) show representative micrographs of the film surface. As observed, each film exhibits a bimodal grain distribution, with smaller primary grains and larger secondary grains. As the film thickness increases, both the primary and secondary grains grow in size, which may be attributed to Ostwald ripening that allows certain grains to grow at the expense of others.

ImageJ to perform measurements of the average grain width. Figure S1 (e)–(h) show histogram plots used to determine the average grain sizes for all the films (see Figure 1(b) in the main manuscript, where we plot the averaged grain sizes across all the AlCu films).

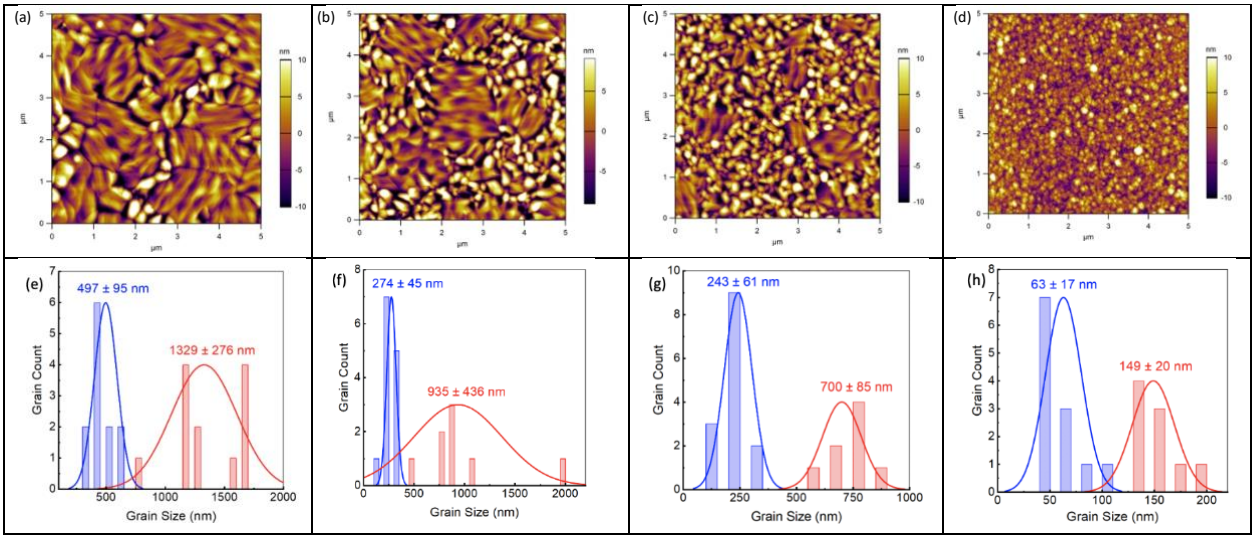

Figure S1. Bimodal grain distribution in AlCu films Representative AFM micrographs used to calculate grain sizes are shown for the (a) 174 nm (b) 98 nm (c) 53 nm, and (d) 24 nm AlCu films. Histograms depicting grain size calculations are shown in the (e) 174 nm, (f) 98 nm, (g) 53 nm, and (h) 24 nm films. All films show the presence of primary (smaller grains, depicted in blue) and coalesced grains (larger grains, depicted in red). Grain sizes were determined using ImageJ.

1. Crystallographic Texture Characterization

X-ray diffraction (XRD) was used to characterize the phase and texture of the films. Diffractograms were collected in a 2θ-ω out-of-plane geometry using a Rigaku SmartLab diffractometer equipped with Cu-Kα radiation (Rigaku Corporation, Akishima-shi, Tokyo,

Japan). Peak widths and positions were analyzed using the LIPRAS software.[1] The XRD results, shown in Figure S2, reveal a single prominent peak from the AlCu film at $2\theta \approx 38.5°$, indicating that the three thicker films are textured with the (111) plane oriented parallel to the sample surface. This is consistent with the AlCu films commonly used in the metal stacks for AlScN and AlN growth. The 24 nm film, however, does not exhibit the same texturing. Please not that given the isotropic nature of thermal transport in AlCu alloys, variations in crystallographic texture are not expected to significantly influence the measured in-plane thermal conductivity in this film. The remaining peaks are attributed to the underlying silicon substrate. Presenting the reference diffraction pattern for crystalline SiO_2 is indicative of the amorphous characteristic of the dielectric layer.

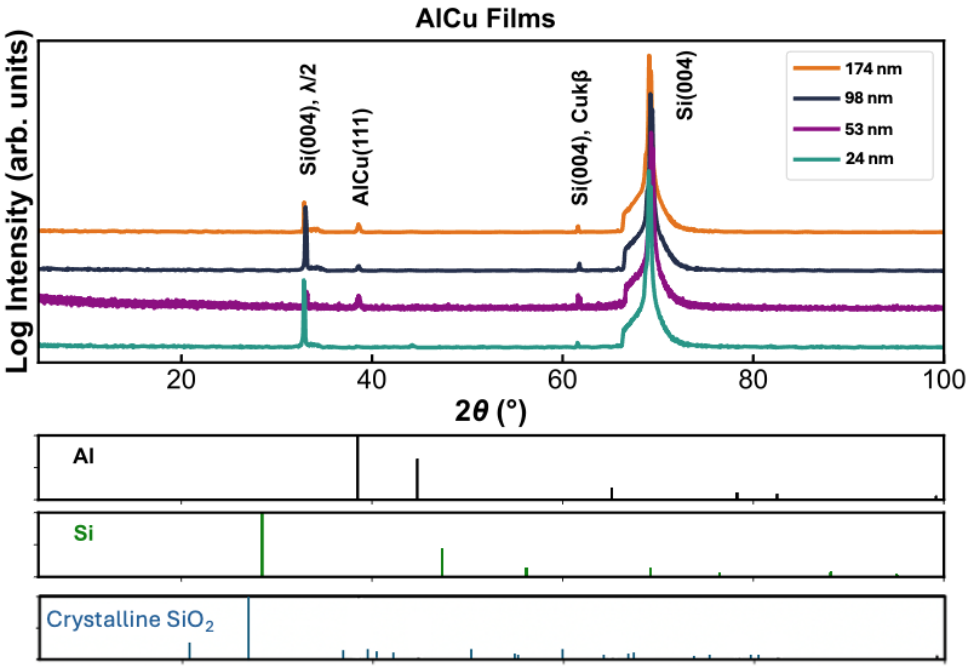

Figure S2. Crystallographic texture in AlCu films X-ray Diffraction (XRD) results demonstrating the peak from all four AlCu films at $2\theta \approx 38.5°$ is shown. This indicates that films with thicknesses ≥ 53 nm exhibit a predominant (111) orientation, whereas the 24 nm film does not display the same texturing.

Supplementary Note 2. Time-Domain Thermoreflectance (TDTR) Experimental Details

Our experimental setup is based on a Ti:sapphire oscillator that emits sub-picosecond laser pulses at a repetition rate of 80 MHz and a central wavelength of ~800 nm. The pump and probe beams are spectrally separated in a two-tint configuration and focused onto the sample surface with equal spot sizes, characterized by a $1/e^2$ spot radius (ω_0). The probe beam is time-delayed relative to the pump beam using a mechanical delay stage, covering a time domain from –15 to 5500 ps. The pump beam is modulated at a frequency (f_{mod}) using an electro-optic modulator with a 50% duty cycle square waveform. We analyze the negative ratio of the in-phase (V_{in}) and out-of-phase (V_{out}) voltage signals that are collected by a fast-response balanced photodetector

as a function of pump-probe time delay, using the 3D multi-layer heat diffusion model developed by Cahill.[2]

We first measure the thermal properties of the SiO_2/Si substrate using TDTR (f_{mod} =8.4 MHz and $\omega_0 = 5.5$ μm after depositing a 73 nm Al transducer. This measurement is sensitive to κ_{SiO_2}, which we fit to a value of $\kappa_{SiO_2} = 1.25$ W m^{-1} K^{-1}. In Table S1, we tabulate parameters used to fit our data collected on the SiO_2/Si substrate.

Table S1. Parameters used to analyze TDTR data (SiO_2/Si) and fit to the thermal model.[3–5]

Material	Thickness (nm)	Thermal conductivity (W m^{-1} K^{-1})	Volumetric heat capacity (MJ m^{-3} K^{-1})	Thermal boundary conductance (MW m^{-2} K^{-1})
Al	73[a]	165[b]	2.42	-
Al/SiO_2 interface	-	-	-	Cannot resolve
SiO_2	1500	**1.25**[c]	1.62	-
SiO_2/Si interface	-	-	-	180
Si	Semi-infinite	140	1.65	-

[a]Measured using picosecond ultrasonics

[b]Measured using four-point probe

[c]**Fit parameter in the measurement**

Next, we utilize concentric two-tint TDTR to measure the in-plane thermal conductivity (κ_r) of all four AlCu films, as detailed below. To maximize sensitivity to κ_r, especially in the thinner films (i.e., at h ≈24 and 53 nm), we perform TDTR measurements directly on the AlCu sample stack without any additional transducer coating. This approach negates the effects of parasitic thermal conductance arising from an added Al transducer layer, which could otherwise reduce sensitivity to κ_r in the underlying AlCu layer. The AlCu metallic layer absorbs photons from the laser, and the resulting thermoreflectance is used as an optical thermometer for our measurements. Consequently, we are insensitive to cross-plane thermal conductivity (κ_z) across all the AlCu films studied.

Furthermore, as stated in the main draft, because the Kapitza length at the AlCu/SiO_2 interface is on the order of 2.5–6.5 nm, well below the thickness of all our AlCu films, we are unable to reliably resolve the thermal boundary conductance across the AlCu/SiO_2 interface, G. The volumetric heat capacity for the dilute AlCu alloy (0.5% Cu) is assumed to be equal to that of Al, at 2.42 MJ m^{-3} K^{-1}[4,5] due to low concentration of Cu. We uniquely quantify the spot size for each measurement using a pump-beam offset scan on the sample surface (as explained in Supplementary Information Note 5). Thus, every unknown parameter is accounted for, except for κ_r, which remains our sole fitting parameter in the thermal model.

Table S2. Parameters used to analyze TDTR data and fit to the thermal model.[3,4,6]

Material	Thickness (nm)	Thermal conductivity (W m^{-1} K^{-1})	Volumetric heat capacity (MJ m^{-3} K^{-1})	Thermal boundary conductance (MW m^{-2} K^{-1})
AlCu Film	24, 53, 98, 174	**To Fit**[a]	2.42	-
AlCu/SiO_2 interface	-	-	-	Cannot resolve
SiO_2	1500	1.25	1.62	-
SiO_2/Si interface	-	-	-	180
Si	Semi-infinite	140	1.65	-

[a]**Fit parameter in the measurement**

Measurement details for each film are provided below:

1. 174 nm AlCu film:

An important consideration when fitting data for the 174 nm AlCu film is the thermal response time required for longitudinal heat gradients to equilibrate within the relatively thick AlCu layer. This time is characterized by $\tau \approx hC/G$, where h is the film thickness, C is the volumetric heat capacity, and G is the estimated thermal boundary conductance at the AlCu/SiO_2 interface.[7] Using $h \approx 174$ nm, $C \approx 2.42$ MJ m^{-3} K^{-1}, and $G \approx 500$ MW m^{-2} K^{-1} we estimate $\tau \approx 850$ ps. As shown in the sensitivity curves in Figure S3. (b), the sensitivity to κ_z approaches zero beyond ~300 ps. Accordingly, accurate fitting of κ_r can only be performed after this time. To ensure reliable results, we initiate data fitting from 500 ps and show exemplar model fits in Figure S3. (a), yielding a κ_r value of 217 W m^{-1} K^{-1}.

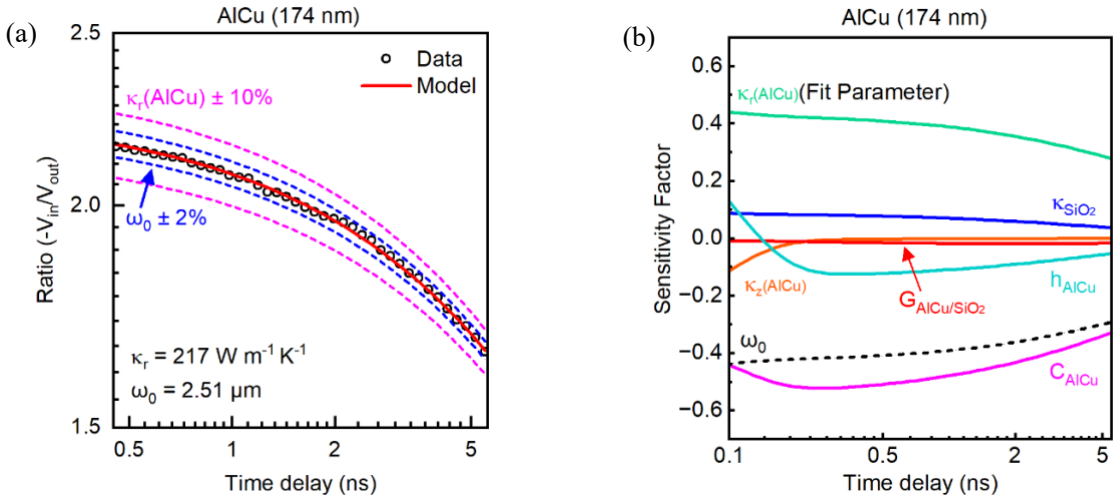

Figure S3. TDTR analysis of the 174 nm AlCu Film (a) Datasets showing fits to κ_r with 10% confidence bounds indicated by dashed pink lines. Measurements are conducted with a spot size ω_0 =2.51 μm, accurate within a 2% deviation (as explained in Supplementary Information Note 5). The 2% confidence bounds are also shown as dashed blue lines. (b) Sensitivity plots are presented, highlighting regions where the measurement is most sensitive to κ_r and ω_0.

2. 98 nm AlCu film:

This is a standard TDTR measurement, where, after verifying the spot size, we fit for κ_r and obtain values as shown in Figure S4 (a). The associated sensitivity plots are shown in Figure S4 (b).

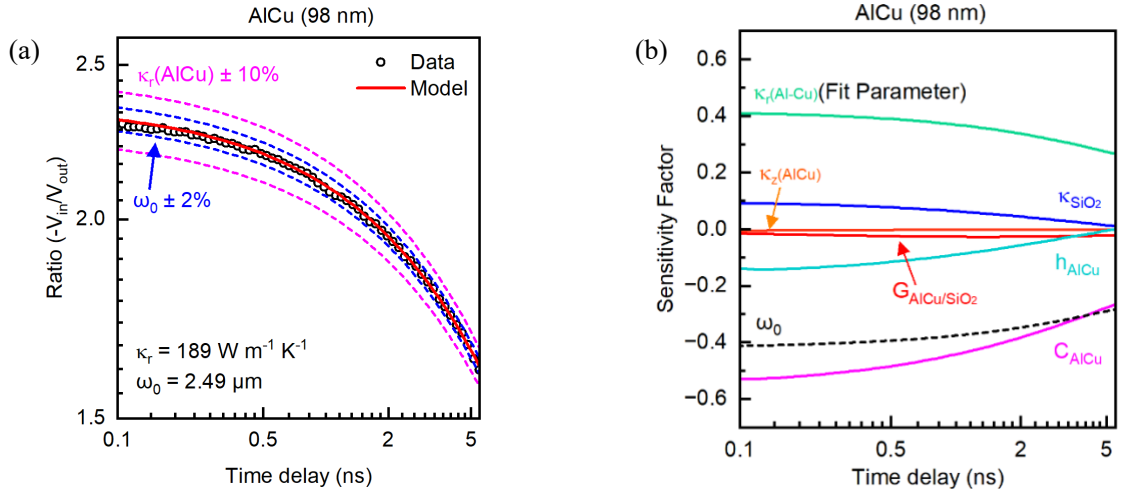

Figure S4. TDTR analysis of the 98 nm AlCu Film (a) Datasets showing fits to κ_r with confidence bounds of 10% shown in dashed pink lines. Measurements are carried out with a spot size $\omega_0 = 2.49$ μm, accurate to within a deviance of 2% (as explained in Supplementary Information Note 5). The confidence bounds of 2% are also shown in dashed blue lines. (b) Sensitivity plots are shown where the measurement is maximally sensitive to κ_r, ω_0.

3. 53 nm and 24 nm AlCu film:

To accurately fit the 53 nm and 24 nm AlCu films, it was necessary to incorporate a "super-absorbing" AlCu layer assumption into our thermal model, as explained by Cahill in Ref.[2] This layer mimics the absorption of laser photons within the optical "skin" depth, resulting in a non-equilibrium hot electron distribution in the top few nanometers of the metallic AlCu film. We account for this "super-absorbing" layer by adding a 1.5 nm thick layer (for the 53 nm film) and a 0.7 nm thick layer (for the 24 nm film), with ten times the volumetric heat capacity ($C \approx 24.2$ MJ m^{-3} K^{-1}) and ten times the thermal conductivity ($\kappa_r \approx 1600$ W m^{-1} K^{-1} for the 53 nm film and $\kappa_r \approx 980$ W m^{-1} K^{-1} for the 24 nm film). By doing so, we find that our datasets fit the thermal model, as shown in Figure S5. (a) and (c), along with the associated sensitivity plots in Figure S5. (b) and (d).

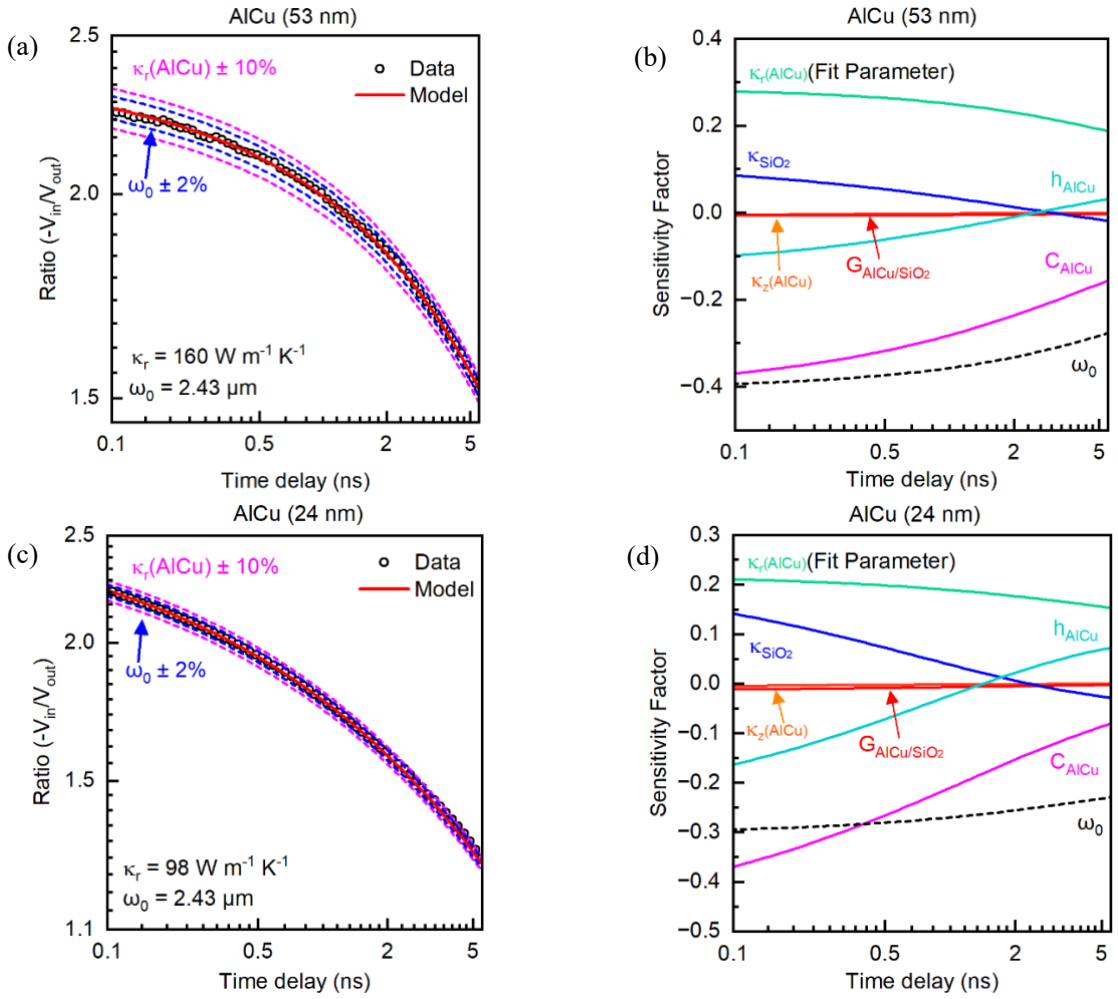

Figure S5. TDTR analysis of the 53 and 24 nm AlCu Films Datasets showing fits to κ_r in (a) a 53 nm film and (c) a 24 nm film, with 10% confidence bounds indicated by dashed pink lines. Measurements are carried out with a spot size of $\omega_0 = 2.43$ μm, accurate within a 2% deviation (as explained in Supplementary Information Note 5). The 2% confidence bounds are also shown as dashed blue lines. (b) and (d) present sensitivity plots for the 53 nm and 24 nm films, respectively, highlighting regions where the measurement is most sensitive to κ_r and ω_0.

Supplementary Note 3. Pump Beam-Offset TDTR Experiment Details

To further validate the in-plane thermal conductivity of the two thinnest AlCu films (24 nm and 53 nm), we employ a time-domain thermoreflectance (TDTR) technique with offset pump-probe. The beam offset pump-probe has an advantage over concentric pump-probe wherein the measurement becomes insensitive to the interfacial boundary conductance (G) between the thin film and the underlying substrate, as well as other cross-plane thermal gradients in the sample stack. This reduces measurement uncertainties propagating from G.

To be able to offset the pump beam, with respect to a stationary probe beam, we attach piezo motors to a mirror on the pump path, which is set to move at a specific angle. Moving the pump beam by that angle offsets the beam position on the sample by a correlated distance. This distance is measured using an optical ruler, imaged on a camera, and converted to micrometers.

Thus, we obtain a calibration of radians to micrometers – i.e., moving the mirror by a certain angle will correlate with a certain distance traversed by the beam on the sample. Care was taken to ensure that there is no clipping of the pump beam during the offset technique, through camera imaging. Using an infinity corrected long working distance 50× objective lens, we find that we are able to reliably offset the beam to 10 µm without any noticeable clipping or beam distortion. This, as we show below in our plots, is within the range and resolution of our measurement.

We first measure the laser $1/e^2$ spot size of the 50× objective lens using pump beam offset. This measurement is performed at a high modulation frequency of 8.4 MHz and at a pump-probe time delay of +100 ps. The full-width at half-maximum (FWHM) of the phase-corrected in-phase signal (V_{in}) is the laser spot size at 50× and is measured to be ~1.67 µm. Next, we perform another measurement at a lower modulation frequency of 1.1 MHz and at a pump-probe time delay of -100 ps. The FWHM of the phase-corrected out-of-phase signal (V_{out}) provides the lateral extent of heat spreading in the sample, and the fit yields the in-plane thermal conductivity, per the method outlined by Feser et al. in Ref.[8] Below, we plot our datasets in Figure S6 for the 53 and 24 nm AlCu films.

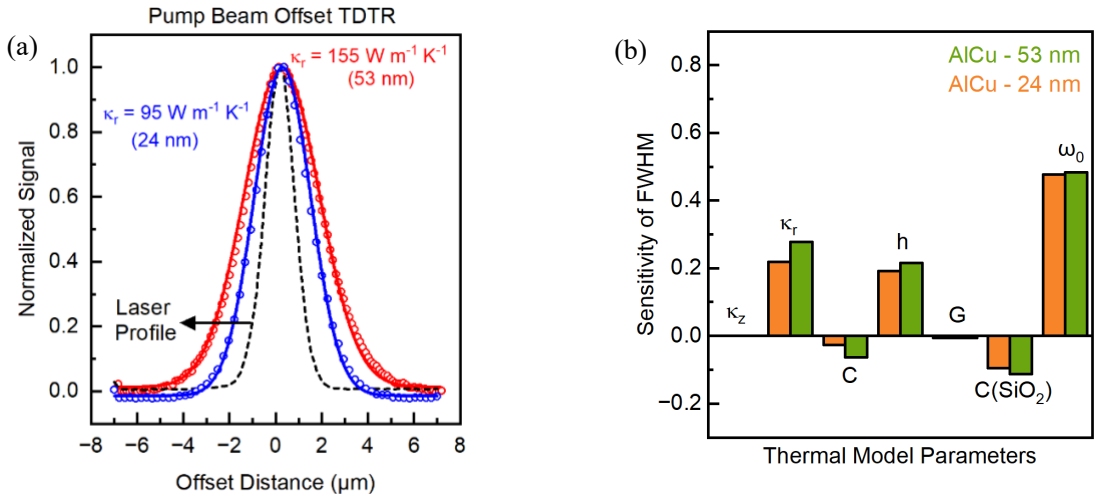

Figure S6. Beam offset analysis (a) Beam offset analysis of the 53 nm and 24 nm films. (b) Sensitivity to parameters in the beam offset measurement for both 53 nm and 24 nm AlCu films. Unless otherwise noted, all parameters used to compute the sensitivity of the FWHM pertain to the AlCu layer. G denotes the thermal boundary conductance between AlCu and SiO_2. Sensitivity analyses are performed for the FWHM of the V_{out} signal at –100 ps for scans taken at 1.1 MHz.

In Figure S6, unless otherwise noted, all parameters used to compute the sensitivity of the FWHM pertain to the AlCu layer. G denotes the thermal boundary conductance between AlCu and SiO_2. Sensitivity analyses are performed for the FWHM of the V_{out} signal at –100 ps for scans taken at 1.1 MHz. We note that the measurement is highly sensitive to spot size. It exhibits positive sensitivity to κ_r in the AlCu film and negative sensitivity to the heat capacity C of both the AlCu and SiO_2 layers. This trend can be broadly attributed to the FWHM being sensitive to the radial thermal diffusivity, κ/C, of the stack. The measurement is also sensitive to the

thickness of the AlCu layer but insensitive to all cross-plane thermal conductances in the sample stack, including κ_z of AlCu and SiO_2.

Supplementary Note 4. Time-Resolved Magneto-Optic Kerr Effect (TR-MOKE)

The magneto-optic Kerr effect (MOKE) refers to the change in the polarization of light reflected from a magnetic surface, directly related to the material's magnetization, which scales linearly with temperature. Upon laser irradiation, the non-equilibrium ultrafast magnetization response persists for ~1–5 picoseconds, after which photo-excited carriers thermally relax, and heat conduction dominates energy transfer. In a pump-probe optical setup, the thermo-magnetic signal from time-resolved MOKE (*dM/dT*) is analogous to the thermoreflectance signal from TDTR (*dR/dT*) and can be used to extract thermophysical properties and track nanoscale heat transfer across interfaces.

As discussed in the main text, TR-MOKE can be reliably performed using optically semi-transparent magnetic transducers (e.g., ~10 nm of Co-Pt, with a thermal conductivity (κ) of ~15–20 W m^{-1} K^{-1} and a volumetric heat capacity (C_v) of ~2.92 MJ m^{-3} K^{-1}). The radial conductances and thermal masses of Al, Co-Pt, and AlCu are summarized in Table S3. A qualitative comparison between the two transducers reveals that the radial conductance of a ~15 nm Co-Pt film is lower than that of an ~80 nm Al film by a factor of ~50, while the thermal mass is lower by a factor of ~4.5. Similarly, compared to a 24 nm AlCu film, the radial conductance of Co-Pt is lower by a factor of ~10, and the thermal mass is lower by a factor of ~1.5. These observations indicate that when using a Co-Pt transducer, the in-plane heat current remains largely confined within the AlCu layer over the ~6 ns time window of the MOKE experiment. Therefore, the TR-MOKE measurements performed with a carefully designed Co-Pt multilayer transducer not only enhance sensitivity to the in-plane thermal properties of the underlying 24 nm AlCu film but also improve the temporal resolution of the scan.

Table S3. Calculated radial thermal conductance as well as thermal mass for a typical Al TDTR transducer, the Co-Pt MOKE transducer used in our experiment, and the underlying AlCu thin film of interest. Here h denotes the thickness in nm, κ_r is the in-plane thermal conductivity and C_v is the volumetric heat capacity. Radial thermal conductance is defined as thickness times in-plane thermal conductivity and thermal mass is defined as thickness times volumetric heat capacity.

Material	h (nm)	$h \times \kappa_r$ (W K^{-1})	$h \times C_v$ (J m^{-2} K^{-1})
Al	80	11200×10^{-9}	192×10^{-3}
Co-Pt	15	225×10^{-9}	43.8×10^{-3}
AlCu	24	2400×10^{-9}	57.6×10^{-3}

1. Description of the TR-MOKE Apparatus

Our TR-MOKE experimental setup is built around a Ti:sapphire oscillator (Tsunami, Spectra-Physics) that outputs a sub-picosecond pulsed laser beam (repetition rate ~80 MHz, central wavelength ~800 nm, FWHM ~11 nm). This beam is split using a polarizing beam splitter into a pump and a probe beam, which are further spectrally separated using ultrafast steep-edged

optical filters (Semrock filters, AVR Optics), enabling a two-tint measurement configuration. The probe path includes a short-pass filter, while the pump beam is optically chopped using a long-pass filter. The pump beam is modulated with a 50% duty cycle at a frequency f_{mod} using an electro-optic modulator (Model 350-160 EOM and 25D amplifier, Conoptics) with square-wave modulation. The probe beam is delayed relative to the pump beam by means of a mechanical delay stage, enabling time-domain measurements from -15 ps to 6 ns. The linearly polarized pump and probe beams are concentrically focused onto the sample using either a 10× objective lens (yielding a 1/e^2 radius of 5 μm) or a 20× objective lens (1/e^2 radius of 2.3 μm) for MOKE measurements.

The reflected pump and probe beams are passed through a 50:50 beam splitter and directed towards another steep-edged short-pass optical filter, oriented at the same angle as the filter on the probe path. This ensures that the entirety of the reflected pump is rejected, while the majority of the reflected probe is passed through to a λ/2 waveplate and a Wollaston prism, where it is split into orthogonal polarizations ('*s*' and '*p*'). Each of the two polarized beams is focused onto the two inputs of a balanced Si photodiode. As shown in Figure S7, we employ a mirror–knife-edged prism combination to ensure that the path lengths of the two polarized beams are identical, avoiding signal artifacts. Furthermore, the λ/2 waveplate is rotated so that the DC voltage signals on each input of the balanced photodiode are equal, resulting in a DC voltage output of zero. This ensures that the AC voltage output from the balanced photodetector is free of DC artifacts and is predominantly proportional to the thermo-magnetic response of the reflected probe beam. The AC voltage signal is then read by a radio-frequency lock-in amplifier (model HF2LI, Zurich), set to reference frequency of f_{mod}. The output from the lock-in amplifier includes in-phase (V_{in}) and out-of-phase (V_{out}) components. The negative ratio of the in-phase and out-of-phase components, ($-V_{in}/V_{out}$), is used for data interpretation and analysis as a function of pump-probe time delay.

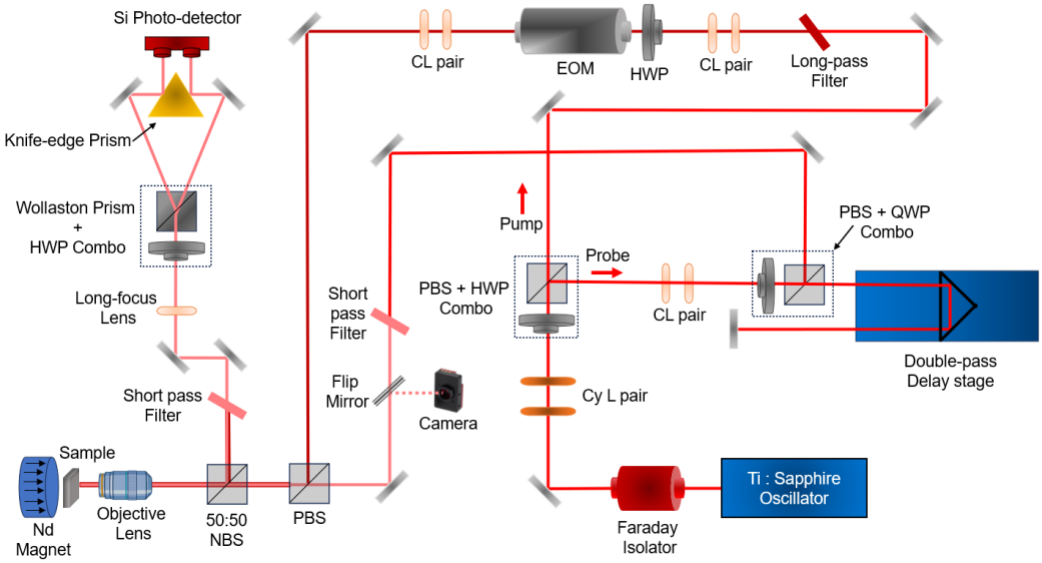

Figure S7. Schematic of TR-MOKE setup at the University of Virginia

2. Material Characterization of the Co-Pt Magnetic Transducer

We perform TR-MOKE in a polar-MOKE configuration, which requires the magnetic moments in the transducer to be saturated out-of-plane throughout the scan, according to the standard Voigt configuration. However, in most thin ferromagnetic films, the magnetic moments naturally tend to orient in-plane. Therefore, the in-plane moments must be fully canted out-of-plane before conducting a TR-MOKE measurement to ensure a strong signal-to-noise ratio (SNR). This enables fitting the data to the 3D heat diffusion model, following the Feldman algorithm to extract the thermal properties. Note that, unless the magnetic moment of the transducer is fully saturated, the obtained MOKE signals will not yield a reliable fit to the Feldman algorithm. In the case of strong ferromagnetic transducers, such as Co and Fe, the saturation magnetization moment M_s is typically around 1.5–2.3 Tesla, and it is difficult to orient out-of-plane without the use of powerful water-cooled electromagnets. However, carefully engineered Co-Pt multilayers, with a stack geometry as depicted in Figure S8 (a), can yield effective out-of-plane perpendicular magnetic anisotropy (PMA) and provide saturation of moments at reasonable external magnetic fields of 0.02 T, as shown in our vibrational sample magnetometry (VSM) data, taken at 300 K in Figure S8 (b). Thus, these transducers yield excellent SNR with the use of simple NdFeB permanent magnets and are ideal for polar-MOKE measurements.

Our multilayer Co-Pt transducers were deposited directly onto clean samples using radio frequency (RF) sputtering in an ultra-high vacuum magnetron sputtering chamber, at room temperature, from elemental Co and Pt targets. The base pressure was 1.3×10^{-5} Pa. The Ar deposition pressure was 1.3 Pa. The deposition rates were 0.12 nm/s and 0.10 nm/s for Co and Pt, respectively. The deposition rates were calibrated from a thicker Co film and a thicker Pt film (~50 nm on SiO_2/Si) using X-ray reflectometry.

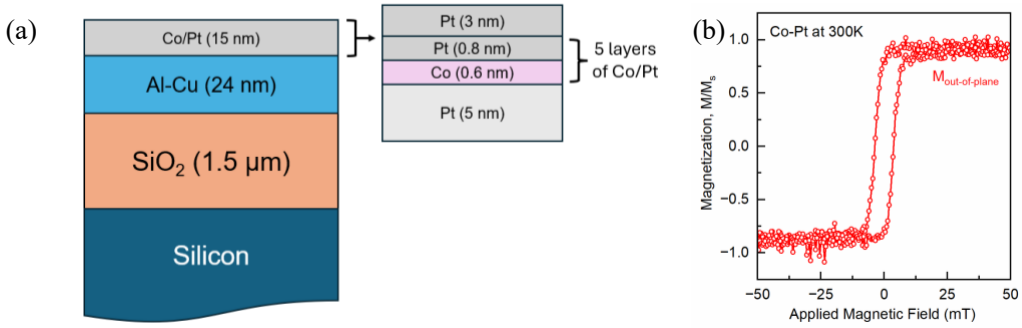

Figure S8. Sample Characterization (a) Sample geometry with Co-Pt transducer. (b) Out-of-plane magnetic hysteresis loop of Co-Pt film on a SiO_2/Si substrate, measured using a vibrational sample magnetometry (VSM) apparatus, with an external applied magnetic field applied along the out-of-plane direction, at 300K. The VSM datasets confirm perpendicular magnetic anisotropy (PMA) in the Co-Pt multilayer, where the Y axis shows the magnetization ratio of the magnetic moment (M) to the saturated magnetization (M_s) against the applied magnetic field, shown in the X axis. A ratio of ±1 indicates saturation of moments in the ± orientation.

3. TR-MOKE Experiment and Description of Signals

Despite the use of a balanced photodiode, the AC voltage signal obtained from a TR-MOKE experiment almost always includes spurious background artifacts. To resolve this, MOKE scans

are typically performed twice – with the out-of-plane transducer moments first aligned in the North ($+M$), and then subsequently in the South ($-M$) directions. This orthogonal switching of transducer magnetic moments is achieved through the use of a NdFeB permanent magnet. We demonstrate this in Figure S9 (a), where we plot the resultant phase-corrected $V_{in}(t)$ and $V_{out}(t)$ signals in both ($\pm M$) orientations, as a function of time delay, for the 24 nm AlCu film. Note that the reversal of the in-phase and out-of-phase signals upon field switching, which indicates that the transducer magnetic moment is, indeed, flipped in the opposing orientations. The resultant MOKE signals, $V_{in}^{MOKE}(t)$ and $V_{out}^{MOKE}(t)$, plotted in Figure S9 (b), are obtained by subtracting the in-phase and out-of-phase signals at ($+M$) and ($-M$) fields. This eliminates signal artifacts that are unrelated to MOKE. Specifically, $V_{in}^{MOKE}(t) = V_{in}^{+}(t) - V_{in}^{-}(t)$ and $V_{out}^{MOKE}(t) = V_{out}^{+}(t) - V_{out}^{-}(t)$.

The negative ratio, $-V_{in}^{MOKE}(t)/V_{out}^{MOKE}(t)$, when plotted in the time domain, can be fit using the 3D heat diffusion model, and is analogous to the TDTR ratio, albeit with greater temporal resolution and scan sensitivity, meaning, we are able to begin fitting the signal from a time delay of ~30 ps. It is worth re-emphasizing that unless the transducer moments are fully saturated in both directions for the entire duration of the MOKE measurement, the resulting dataset will not yield a reliable fit to the thermal model.

Determining the accurate thickness of the transducer is crucial when performing thin film MOKE measurements. This is primarily due to the sensitivity of the signal ratio ($-V_{in}/V_{out}$) to transducer thickness on par with the sensitivity to the thermal properties of the underlying thin film substrate. This is also due to the thermal mass of the Co-Pt transducer being comparable with the thermal mass of the AlCu film. However, unlike in Al transducers used for TDTR, where picosecond acoustics is a reliable way of obtaining the film thickness,[9] the Co-Pt multilayer used for TR-MOKE does not produce sharp acoustic echoes at short time delays. Moreover, estimating the longitudinal sound speeds for a multilayer is not a trivial pursuit. Thus, to measure the thickness of the Co-Pt transducer, we utilize two calibration substrates, BK-7 and Al_2O_3, with known thermal properties, and fit for the thickness of the transducer. These measurements yield a transducer thickness of 16$\pm$1.5 nm. The volumetric heat capacity, C_v, of the transducer film, which we estimate using the weighted average of the heat capacities of Co and Pt, is ~2.92 MJ m^{-3} K^{-1}, that is comparable with that used in Ref.[10] We estimate the thermal conductivity of the Co-Pt transducer using the four-point probe apparatus. We measure the sheet resistivity of the transducer, convert to electrical conductivity, and use the Wiedemann-Franz law to obtain the electronic thermal conductivity of the film to be 16$\pm$1.3 W m^{-1} K^{-1}.

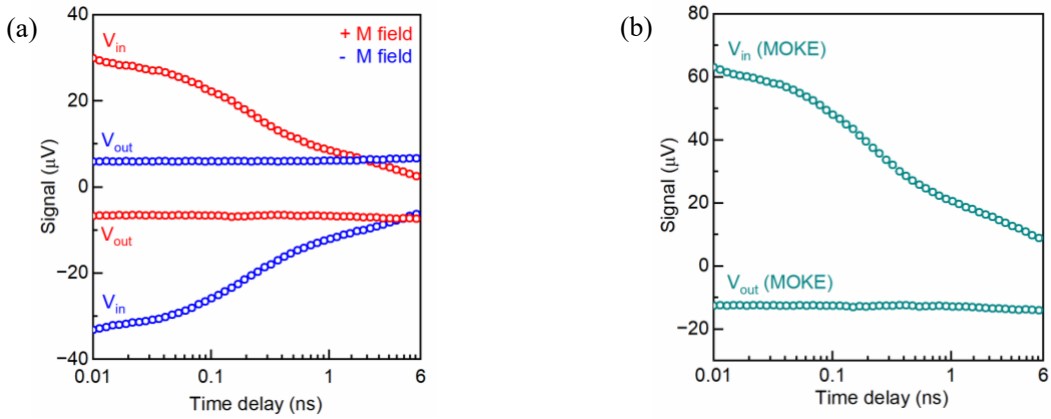

Figure S9. TR-MOKE Representative Signals (a) Phase-corrected V_{in} and V_{out} signal at $\pm M$ fields, obtained from a sample stack of Co-Pt (16 nm)/AlCu (24 nm)/SiO_2 (1.5 μm)/Silicon at f_{mod} of 8.4 MHz and a $1/e^2$ spot radius of 5 μm, and (b) the resultant V_{in} (MOKE) and V_{out} (MOKE) signals, obtained from subtracting the orthogonal V_{in} and V_{out} signals at $\pm M$ fields, are plotted as a function of pump-probe time delay.

4. Frequency-Dependent Variable Spot size TR-MOKE for In-plane Thermal Conductivity

Modulating the pump beam frequency (f_{mod}) influences the thermal gradient distribution in both cross-plane and in-plane directions. At elevated (f_{mod}), heat transport becomes quasi-one-dimensional along the cross-plane axis, enhancing sensitivity to the cross-plane thermal conductivity of the underlying film and the thermal boundary conductance at the film–transducer interface. At lower modulation frequencies, the thermal penetration depth, defined as $d = \sqrt{\frac{k_r}{\pi . f_{mod} . C_v}}$, increases in both the cross-plane and in-plane directions, and the MOKE ratio becomes progressively more sensitive to the in-plane thermal conductivity of the film. When MOKE is performed at low frequencies with a smaller spot size - such that the $1/e^2$ radius is smaller than the in-plane thermal penetration depth- heat transport becomes three-dimensional, significantly enhancing sensitivity to the substrate's in-plane thermal properties.

MOKE measurements were performed at two modulation frequencies: (i) 8.4 MHz with a $1/e^2$ radius of 5 μm, and (ii) 1.1 MHz with a $1/e^2$ radius of 2.3 μm. At f_{mod}= 1.1 MHz, the in-plane thermal penetration depth d is 3.55 μm, exceeding the spot radius (ω_0= 2.3 μm), confirming the suitability of this modulation frequency for the measurement. The spot size was determined using a pump-beam offset method (described in detail in the Beam Offset section). The MOKE ratio and corresponding thermal model fits are shown in Figure S10 (a) and (c), while the measurement sensitivities are presented in Figure S10 (b) and (d).

Table S4. Parameters used to fit the MOKE ratio signal to the 3D heat equation

Material	Thickness (nm)	Thermal conductivity, κ_r (W m^{-1} K^{-1})	Thermal conductivity, κ_z (W m^{-1} K^{-1})	Volumetric heat capacity (MJ m^{-3} K^{-1})	Thermal boundary conductance (MW m^{-2} K^{-1})
Co-pt	16	16	16	2.92	-
Co-Pt/AlCu interface					**To Fit**
AlCu Film	24	**To Fit**	**To Fit**	2.42	-
AlCu/SiO_2 interface	-	-	-	-	133
SiO_2	1500	1.25	1.25	1.62	-
SiO_2/Si interface	-	-	-	-	180
Si	Semi-infinite	140	140	1.65	-

The thickness of the Co-Pt layer was estimated using MOKE measurements on BK-7 and Al_2O_3 calibration samples, with a measurement uncertainty of 10%. The interfacial thermal conductances, G_2 and G_3, as well as the isotropic thermal conductivities of the SiO_2 and Si layers were determined using transducer-less TDTR measurements. The volumetric heat capacities for each layer are taken from literature. Thus, the three unknown parameters that we need to fit for, are: the thermal conductance, G_1, between the Co-Pt and AlCu interface, and κ_z and κ_r of the AlCu film.

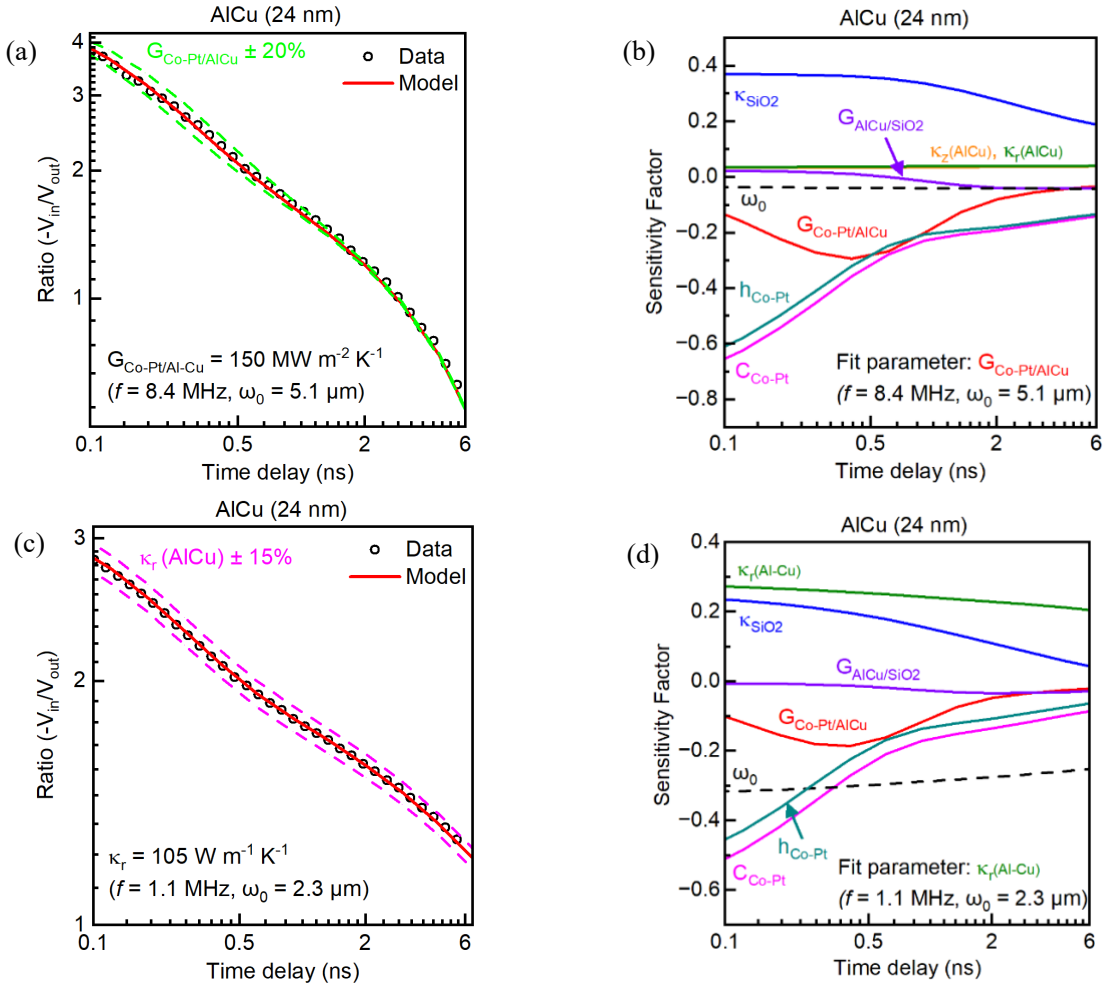

Figure S10 TR-MOKE Data Analyses and Sensitivity (a) and (c) show plots of the experimental data in black open circles at f_{mod} of 8.4 MHz and at 1.1 MHz and ω_0 of 5.1 μm and 2.3 μm, respectively, along with the best fit to the 3D diffusion model in solid lines in red. The dashed blue lines represent the perturbed G_1 value by ± 20% and κ_r by ± 15%. (b) and (d) show sensitivity of the ratio to the measurement parameters at f_{mod} of 8.4 MHz sensitive to G_1 and 1.1 MHz sensitive to κ_r, respectively.

At f_{mod}=8.4 MHz and ω_0 =5 μm, the ratio is highly sensitive to G_1; thus, we fit for G_1. We demonstrate this sensitivity to G_1 by perturbing the value by ±20% and showing deviations in the fit curves, especially at shorter time delays. The sensitivity to κ_z of the 24 nm AlCu film is negligible at higher modulation frequencies, likely due to the fact that for a thin film (thickness = 24 nm), we cannot reliably decouple the cross-plane thermal conductivity from the boundary conductances on either side of the film, thus, effectively generating a "lumped resistance" thermal circuit.

At f_{mod} = 1.1 MHz and ω_0 = 2.3 μm, the ratio becomes significantly more sensitive to κ_z and κ_r of the AlCu film; thus, we treat G_1 as a fixed parameter and fit for κ_z and κ_r. The enhanced sensitivity to κ_r is depicted by perturbing the value by ±15%, and plotting the resulting model shown in dashed pink lines in Figure S10 (c). This methodology yields κ_z= κ_r =105±19 W m^{-1} K^{-1} and G_1 =150±23 MW m^{-2} K^{-1}. This points to thermal isotropy in the 24 nm AlCu film. Thus,

we are able to uniquely determine the cross-plane and in-plane thermal conductivity of the 24 nm AlCu film, as well as the transducer-film interfacial conductance through frequency-dependent variable spot size TR-MOKE measurements.

Supplementary Note 5. Spot Size Characterization

The largest source of uncertainty in our experiments arises from the uncertainties in the spot size. Therefore, we employ a three-pronged approach to characterize the spot size in these measurements, as shown below:

1. We perform a TDTR measurement, at 1.1 MHz and using a 20× infinity corrected long working distance (WD) objective lens, on an Al (111) single crystal purchased from MTI, with a known and calibrated thermal conductivity value of 222 W $m^{-1}K^{-1}$. As shown in the sensitivity analyses below, the measurement is sensitive to κ_r, C, ω_0. Each parameter is accounted for, with the only unaccounted parameter being the spot size. Thus, we are able to uniquely fit for the spot size to within 5% confidence bounds, as shown in the Figure S11 (a) below.
2. In addition, we perform a pump beam offset scan at a high modulation frequency (8.4 MHz) at a positive time delay (i.e., +100 ps), where we utilize the phase-corrected V_{in} signal, to measure the $1/e^2$ Gaussian laser spot size, as shown in Figure S11 (c) below.
3. Lastly, we perform TDTR and TR-MOKE calibration measurements on substrates with known thermal conductivities (such as Al_2O_3 and SiO_2) and estimate ω_0.

We see that all our values for ω_0 are within 5% of each other using these three techniques, and therefore, the uncertainties propagating from spot size are reduced to within a 5% deviation.

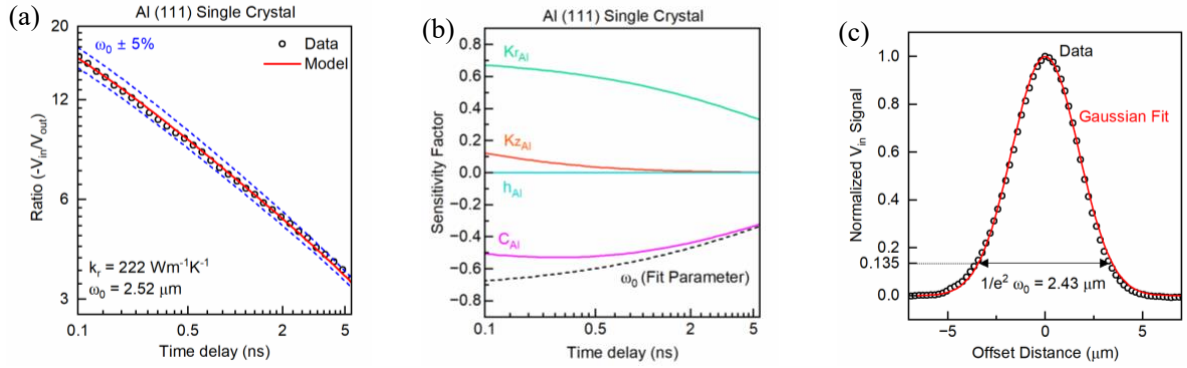

Figure S11. Spot size Characterization (a) Representative datasets for a TDTR measurement on an Al(111) film, taken at $f_{mod} = 1.1$ MHz using 20×, fit to a spot size of 2.52 µm. (b) Sensitivity analyses performed for the measurement. (c) A representative pump beam offset scan performed at $f_{mod} = 8.4$ MHz and a +100 time delay, fit to a $1/e^2$ Gaussian laser spot size of 2.43 µm.

Supplementary Note 6. Ellipsometry Measurements

The ellipsometric data were obtained using IR-VASE (IR-VASE Mark II, J.A. Woollam Company) across the spectral range of 625-5000 cm^{-1} (2-16 µm). Measurements were conducted

at two incident angles of 60° and 70°, with a resolution of 16 cm^{-1}. The effective electron relaxation time in AlCu films was determined through fitted oscillator models applied to the complex frequency-dependent ellipsometric data. The measured ellipsometric values (Ψ and Δ) represent the amplitude ratio and phase difference of the complex reflection coefficients (r_p and r_s) of the sample for *p*- and *s*-polarized light, expressed as $\rho = r_p/r_s = \tan\Psi\, e^{i\Delta}$. Reference values from the literature were employed for the dielectric functions of the silicon substrate and thermal SiO_2 layer.[11] Given their metallic nature, the optical behavior of the AlCu films in the infrared spectrum is predominantly influenced by the free-electron contribution. As such, the Drude free-electron model was utilized to ascertain the optical properties of these films, given by $\varepsilon_{Drude}(\omega) = \varepsilon_1(\omega) + i\varepsilon_2(\omega) = 1 - \omega_p^2/(\omega^2 + i\Gamma\omega)^{-1}$, where ω_p and Γ denote the plasma frequency and the relaxation rate, respectively. Notably, owing to exposure to air, a native oxide layer formed on the top surface, which was modeled using Gaussian oscillators. Parameters for each oscillator model (including the plasma frequency and relaxation rate for the Drude oscillator, as well as amplitude, energy centroid, and broadening for Gaussian oscillators) were optimized to align the model with the collected ellipsometric data by minimizing the mean square error. Finally, the effective electron relaxation time (τ) was derived from the relaxation rate, given as $\tau = \Gamma^{-1}$.

Supplementary Note 7. Four-Point Probe

Electrical Resistivity of the AlCu films were measured with four-point probe technique. For that, we employed a standard four-point probe technique using a Keithley 2612A SourceMeter® system in combination with a Janel probe, which enables high-precision current sourcing and voltage measurement. The probe configuration consisted of a linear array of equidistant tungsten carbide tips spaced 0.5 mm apart. Measurements were conducted on films deposited on 4-inch Si wafers with a 1.5 µm amorphous SiO_2 insulating layer, which eliminated parasitic conduction through the substrate. Each film was measured at least ten times at different locations to account for potential spatial variation, and the reported value reflects the averaged result. The system was calibrated using a standard reference sample prior to measurement. During operation, a constant DC current (4.532 mA) was applied through the outer probes while the voltage drop between the inner probes was recorded with sub-microvolt resolution. At least ten I–V measurements were performed for each sample. Sheet resistance (R_s) was extracted from the I–V measurements, and resistivity was then calculated as $\rho = R_s \times t$, where t is the film thickness determined independently via X-ray reflectometry.

We report the average R_s values of the two different measurements in Table S5.

Table S5. Sheet Resistance from Four-Point Probe Measurements. Each reported value is an average of at least ten separate measurements and R_s has been measured at Sandia National Laboratory after films were grown (second column from the left) and at University of Virginia (fourth columns from the left) prior to thermal conductivity measurements.

Film thickness (Å)	Res (Ω/sq)	Std	Res (Ω/sq)	Std
1737	0.1747	2%	0.1750	2%
977.95	0.3364	1%	0.3356	2%
530	0.6196	2%	0.6163	2%
240	2.3306	3%	2.5320	4%

References:

[1] G. Esteves, K. Ramos, C.M. Fancher, and J.L. Jones, "Line-Profile Analysis Software (LIPRAS)," (2017).

[2] D.G. Cahill, "Analysis of heat flow in layered structures for time-domain thermoreflectance," Review of Scientific Instruments **75**(12), 5119–5122 (2004).

[3] E.A. Scott, J.T. Gaskins, S.W. King, and P.E. Hopkins, "Thermal conductivity and thermal boundary resistance of atomic layer deposited high-k dielectric aluminum oxide, hafnium oxide, and titanium oxide thin films on silicon," APL Mater **6**(5), 58302 (2018).

[4] J.L. Braun, D.H. Olson, J.T. Gaskins, and P.E. Hopkins, "A steady-state thermoreflectance method to measure thermal conductivity," Review of Scientific Instruments **90**(2), 24905 (2019).

[5] X. Zheng, D.G. Cahill, P. Krasnochtchekov, R.S. Averback, and J.C. Zhao, "High-throughput thermal conductivity measurements of nickel solid solutions and the applicability of the Wiedemann-Franz law," Acta Mater **55**(15), 5177–5185 (2007).

[6] P.E. Hopkins, and J.C. Duda, *Introduction to Nanoscale Thermal Conduction* (n.d.).

[7] J. Kimling, A. Philippi-Kobs, J. Jacobsohn, H.P. Oepen, and D.G. Cahill, "Thermal conductance of interfaces with amorphous SiO2 measured by time-resolved magneto-optic Kerr-effect thermometry," Phys Rev B **95**(18), (2017).

[8] J.P. Feser, J. Liu, and D.G. Cahill, "Pump-probe measurements of the thermal conductivity tensor for materials lacking in-plane symmetry," Review of Scientific Instruments **85**(10), (2014).

[9] C. Thomsen, J. Strait, Z. Vardeny, H.J. Maris, J. Tauc, and J.J. Hauser, "Coherent Phonon Generation and Detection by Picosecond Light Pulses," Phys Rev Lett **53**(10), 989–992 (1984).

[10] J.Y. Chen, J. Zhu, D. Zhang, D.M. Lattery, M. Li, J.P. Wang, and X. Wang, "Time-Resolved Magneto-Optical Kerr Effect of Magnetic Thin Films for Ultrafast Thermal Characterization," Journal of Physical Chemistry Letters **7**(13), 2328–2332 (2016).

[11] C.M. Herzinger, B. Johs, W.A. McGahan, J.A. Woollam, and W. Paulson, "Ellipsometric determination of optical constants for silicon and thermally grown silicon dioxide via a multi-sample, multi-wavelength, multi-angle investigation," J Appl Phys **83**(6), 3323–3336 (1998).